Time and temperature dependent softening of a novel maraging steel fabricated by laser metal deposition

Materials & Design 224 (2022) 111393

Contents lists available at ScienceDirect

Materials & Design

journal homepage: www.elsevier.com/locate/matdes

Time and temperature dependent softening of a novel maraging steel fabricated by laser metal deposition

Miwen Yuan [a,b], Lars Nyborg [b], Christos Oikonomou [c], Yicheng Fan [d], Libin Liu [a], Yu Cao [b,*]

[a] School of Materials Science and Engineering, Central South University, Changsha 410083, PR China
[b] Department of Industrial and Materials Science, Chalmers University of Technology, Gothenburg 41296, Sweden
[c] Uddeholms AB, Hagfors 638 85, Sweden
[d] ASSAB Tooling Technology (ShangHai) Co., Ltd, Shanghai 201108, PR China

HIGHLIGHTS

- A novel maraging steel with high hardness was fabricated by the laser metal deposition method for tool steel application.
- The steel was aged for long-term at high temperatures and revealed an outstanding softening resistance.
- Numerical models applied successfully validated the microstructural and property evolution.

GRAPHICAL ABSTRACT

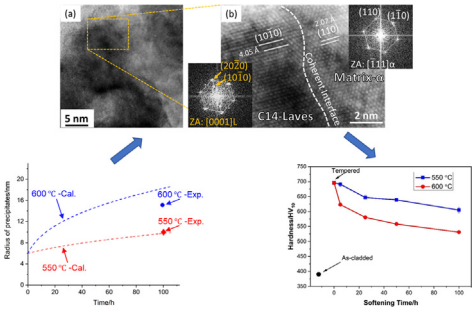

ARTICLE INFO

Article history:
Received 7 September 2022
Revised 7 November 2022
Accepted 17 November 2022
Available online 18 November 2022

Keywords:
Softening resistance
C-14 Laves phase
Coarsening
Simulation

ABSTRACT

Durability is a critical factor for hot stamping dies from an economic point of view. Refurbishing the dies by depositing new material instead of replacement is a promising method to reduce the cost. For this reason, a newly developed maraging steel (NMS) was cladded on a hot work tool steel by means of directed energy deposition. After an optimized tempering, exposures at high temperatures were carried out on the cladded NMS in order to examine the softening resistance. The microstructural evolution of the material was systematically characterized using a combination of optical microscopy (OM), X-ray diffraction (XRD), scanning electron microscopy (SEM), Auger electron spectroscopy (AES) and transmission electron microscopy (TEM). The precipitate in the cladded steel was identified as Laves phase. The coarsening of this phase is considered as the main reason for the thermal softening of the steel at high temperatures. The coarsening behavior was also simulated by using the revised Langer-Schwartz-Wagner (LSW) model, which was in good agreement with experimental observations. Moreover, a mathematical model of precipitate strengthening was successfully applied to evaluate the softening behavior of the steel. This model can be used to predict the hardness/strength evolution of the investigated tool steel during its high-temperature service.

1. Introduction

Hot work tool steels are widely used as die materials, especially in the hot stamping process to fabricate automobile structural components. For the safety of passengers, these structural components should have high strength. In actual applications, one type of boron steel (the grade of 22MnB5) is commonly used for structural components (such as the B-pillar component) due to its relatively low price and high strength obtained after hot forming [1]. However, when hot stamping this high-strength boron steel, the tool steel (the die material) is faced with a harsh environment due to

* Corresponding author.
E-mail address: yu.cao@chalmers.se (Y. Cao).

https://doi.org/10.1016/j.matdes.2022.111393
0264-1275/

the cyclic thermal and mechanical loads, wear, and so on [2]. In this case, the tool steels are required to have combined high hardness, high strength, and decent toughness [34]. The properties of tool steel are significantly influenced by its microstructure. The typical microstructure of hot work tool steel is tempered martensite with secondary carbides. Fine secondary carbides dispersed in tool steel provide sufficient strength/hardness. Regarding the carbides, the Cr-rich M_3C, M_7C_3 and $M_{23}C_6$ carbide often have an easier coarsening tendency compared to the W-rich or V-rich MC carbides [4].

However, due to the high temperature of the steel sheet that die deals with, the carbides in tool steels will be inevitably coarsened at high temperatures, leading to the softening of the die materials [56]. Hence, thermal stable carbides are favorable for hot work tool steel because they can maintain dispersion strengthening effects in materials at elevated temperatures.

Softening of the die can lead to some unexpected failures, such as severe wear, galling phenomenon caused by an accumulative transfer of material from workpieces, progressive worn of tool material and consequently an increase in maintenance costs. The protrusions caused by galling can decrease the surface quality of the components and cause an insufficient heat transfer from the formed sheet to the die, which will again affect the final microstructure and mechanical properties of the formed components. Based on our previous study, all the above issues can be caused by the softening of the tool steel.

In recent years, the development of additive manufacturing (AM) technology provides the possibility to fabricate net-shape components. As one technique of AM, laser metal deposition (LMD) has the advantage on repairing dies and adding new function materials to existing components. For instance, cladding hard materials to the surface of the dies can improve wear resistance. This process is also termed hard facing, a technique that can offer a metallurgical bonding between the deposited coating and the substrate tool. A properly coated surface layer is expected to provide better resistance to wear, corrosion and softening at high temperatures than the substrate.

There are some challenges with the hot work tool steels fabricated by the AM method, such as high cracking susceptibility, and difficulty to form full density parts due to the relatively high contents of carbon and alloy elements used for strengthening the steel and increasing the hardenability. Maraging steels with a carbon-free/low carbon content could be a potential solution for this due to their good weldability.

Maraging steels are usually reinforced by intermetallic precipitates obtained by proper heat treatments. Compared to carbides in common hot work tool steels, these intermetallic phases have a slower growth rate. It is known that the diffusion coefficient of carbon in steel is several orders higher than that of the substitutional alloying elements. As a result, carbides in common hot work tool steels could be coarsened much faster. Generally, minimizing the coarsening rate of the reinforcing phase is one of the major strategies to delay the softening of hot work tool steel at high temperatures. In addition, the precipitate (reinforced particles) coarsening is also driven by the interfacial energy between the precipitate and matrix according to the Langer-Schwartz-Wagner (LSW) model [910]. Usually, high interfacial energy causes a relatively high coarsening rate. Hence, a desired reinforcing phase for hot work steel is supposed to have low interfacial energy with matrix and low diffusion coefficient of the constitutive elements.

Regarding the precipitation hardening behavior of maraging steels, many researchers have studied the mechanical properties and put some effort to model it. Pereloma et al. [7] investigated the dominant strengthening mechanism in a Fe-20Ni maraging steel. It was found that the hardness drops when aging at 550 ℃ for more than 10 min are associated with both the coarsening of the precipitates and the reverse of austenite. However, the strengthening models based on precipitation hardening in the study did not fit the yield strength very well. Pardal et al. [8] also tried to model the precipitation hardening behavior of a type of 18Ni-M300 maraging steel in the 440–650 ℃ range. The results showed that the modeling was only valid until 560 ℃, because the aging at the higher temperatures will cause reversed austenite.

Although maraging steels manufactured by AM have been studied extensively in recent years, most of them are fabricated by laser beam powder bed fusion (LBPF) [111213]. There was limited research related to the LMD process [1415]. The evolution of the microstructure and mechanical property of maraging steel made by LMD during the softening treatments is therefore of great interest. In addition, to the authors' knowledge, the relationship between microstructure and mechanical properties of metallic materials was mostly interpreted in qualitative ways. Quantitative analysis is still insufficient.

The aim of this work is to evaluate the softening resistance of a newly developed maraging steel fabricated by LMD technique at elevated temperatures. The design of low Ni content in this steel aims to avoid reversed austenite, which could lead to the softening of the material. Good softening resistance of this maraging steel is expected because the reinforcing precipitate in this alloy has good thermal stability. The evolution of the microstructure will be simulated by using the LSW model. Furthermore, a quantitative correlation between the microstructure and mechanical properties (specifically, hardness) of this steel will be established.

2. Materials and methods

2.1. Experimental procedure

A newly developed maraging steel (hereafter named NMS) using pre-alloyed feeder stock powder with diameter in the range of 50–150 μm was deposited on a substrate brick of Uddeholm Dievar hot work tool steel without preheating. The nominal compositions of the deposited layer and the substrate are given in Table 1. Samples for this study were produced by a LMD laser printing machine with a Nd:YAG laser beam using a bidirectional scan strategy, where the metal particles are conveyed by argon carrier gas. The deposition was performed on a cladding area of 102 × 52 mm. A constant layer thickness of 1.6 mm was applied to build samples with 1 to 8 layers. The laser power of 1600 kW and the scanning speed of 520 mm/min were kept constant throughout the whole process.

After printing, cubic samples with the size of $10 \times 10 \times 22$ mm^3 were extracted from the cladded bricks. Optimization of the tempering parameters was conducted on the as-cladded samples to yield the material with the highest hardness value. The optimized parameter was identified as double tempering at 535 ℃ for 3 h. To evaluate the softening resistance of the material, the tempered samples were then heat-treated at 550 ℃ and 600 ℃ for 5 h, 25 h, 50 h and 100 h respectively, followed by air cooling to room temperature.

Hardness measurement was performed on the top layer from the polished cross-section of the cubic samples using Struers DuraScan-70 G5. The testing load is 10 Kgf, and the dwell time is 15 s. Six indentations were measured to obtain the average Vickers hardness.

For microstructure analysis, the samples were mounted, ground and polished up to 1 μm diamond suspension and then etched with an etchant constituting 4 % HNO_3 + 4 % HCl. The microstructure of these samples was characterized by means of a Zeiss Axioscope 7 light optical microscope with a model of tiles (interactive) and a Zeiss LEO Gemini 1550 field emission scanning electron

Table 1
Chemical composition (wt.%) of the cladded material (NMS) and substrate (Uddeholm Dievar).

Material	C	Si	Mn	Cr	Mo	Co	Cu	Ni	V	Fe
NMS	0.03	0.35	0.40	5.0	8.0	12.0	2.0	2.0	–	Bal.
Uddeholm Dievar	0.35	0.2	0.5	5.0	2.3	–	–	–	0.6	Bal.

microscope (FEG-SEM). The chemistry of the small precipitates was analyzed by means of a PHI 700 Scanning Auger Nanoprobe. The accelerating voltage of the electron beam is 10 kV, and its beam current is 10 nA. Before the analysis, the oxide and carbon contamination on the sample were removed by a gentle argon ion sputtering. To identify the phases formed, XRD measurements were performed on the top surface of polished cubic samples to avoid the influence of the rough surfaces using a Bruker D8 Advance with a Cr X-ray source. The 2-theta range was 30° – 158° and the step size was 0.05°. In order to investigate the fine precipitates further, a transmission electron microscope (TEM) was also used. Thin-foil TEM samples with 3 mm diameter were prepared by grinding to a thickness of ~ 80 μm and then electrolytic polished using the Struers A2 electrolyte at 2 ℃. The FEI Tecnai T20 TEM was operated at 200 KV. The Digital Micrograph (TM) 3.9.1 software was used to assist in the analysis of TEM images. The particle size and fraction of precipitates were statistically analyzed by ImageJ software from 3 images for each sample. In addition, to complement the experimental observation, simulation to predict the equilibrium phases in the steel was performed by means of Thermo-Calc (2019b) software using the TCFE9 database.

3. Results

3.1. Microstructure evolution

The optical micrographs of the as-cladded NMS with various layers are shown in Fig. 1. Crack-free and nearly full dense cladded zone was obtained even in the sample with 8-layers, suggesting that NMS had excellent weldability. The magnified graph (Fig. 1d) shows a typical martensite structure in the as-cladded steel.

XRD measurements were applied to check the phase constitution of NMS before and after softening (Fig. 2) and α in the figure means bcc/bct-Fe phase. As shown in Fig. 2, only martensitic matrix was detected in the as-cladded sample, indicating little retained austenite. The reason behind this was the low C concentration in this type of steel. Using JMatPro software, the martensite start- and finish-temperature (M_s & M_f) of the material were estimated to be as high as 430 ℃ and 295 ℃ respectively. Consequently, when the steel was fast-cooled from the austenitic region to room temperature, the steel could be completely transformed into martensite and no austenitic phase would be retained. Compared to the as-cladded sample, the α peaks in other three heat-treated samples were shifted towards higher 2θ-angles, implying the decomposition of martensite during tempering. In addition, no reverted austenite was found in the tempered or softened samples, although it has been frequently found in other types of maraging steel after high-temperature tempering [161718]. Notice that in general maraging steels, high content of Ni (17–19 wt%) makes the austenite phase more stable, and part of the martensite will be reverted to the austenite phase at high temperatures. The low nickel content (~2 wt%) of the maraging steel in this study (NMS) resulted in a relatively small austenite region in the phase diagram and consequently the absence of reverted austenite in the tempered samples. This was beneficial to the high hardness. In Fig. 2, no difference was observed from the XRD pattern in these three heat-treated samples. Moreover, peaks of the expected precipitates were not found neither. Only two humps were barely seen, one was located at the left of the (110) peak

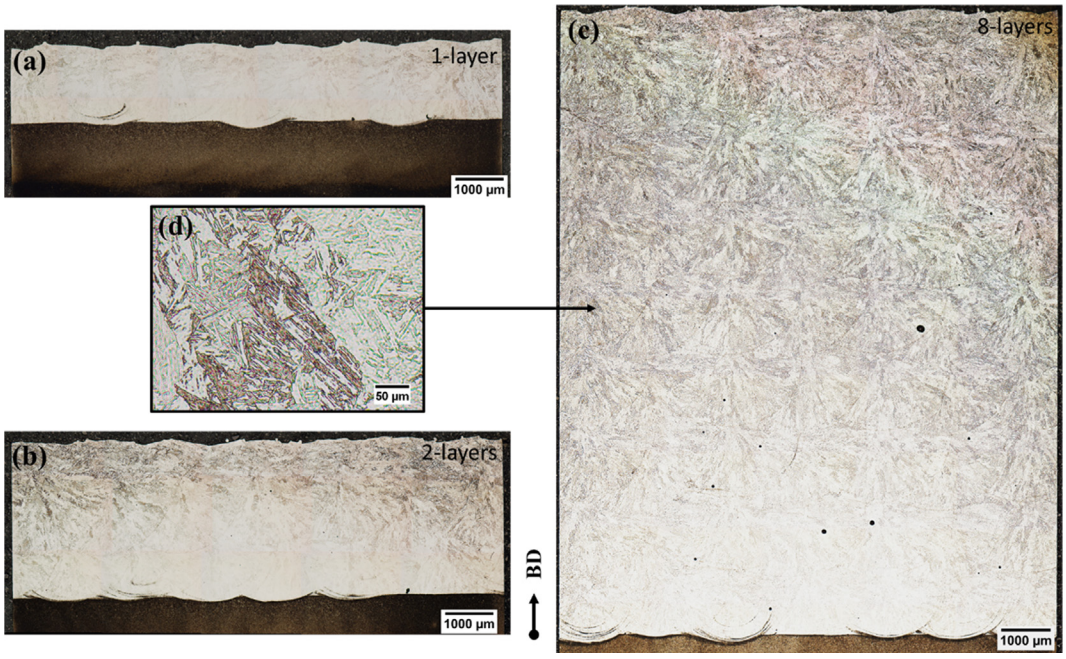

Fig. 1. The optical micrographs of as-cladded NMS (cross-section) with: (a) 1-layer, (b) 2-layers, and (c) 8-layers; (d) The magnified graph exhibits the typical martensite structure.

and another was between 2-theta of 120–140°. Notice, these humps were not observed in the as-cladded sample and were expected to be from some nano precipitates in heat-treated samples.

The microstructure between different cladding layers had no distinct difference. Only the bottom layer had more primary carbide particles along the grain boundaries. This was probably due to the dilution effect from the substrate material, which leads to the increase of C concentration in the bottom layer. Therefore, the microstructure evolution in the top layer was selected to be shown in this study. Fig. 3 illustrates the microstructure from the cross-section of the top layer by SEM before and after heat treatments at different conditions. As exhibited in Fig. 3a, no precipitate but a few primary carbides were found along the prior austenite grain boundary in the as-cladded sample. The morphology within the grains was probably caused by the different orientations of the martensite structure. Precipitates were also absent in other layers, indicating that the intrinsic heat treatment effect from the subsequent deposition to previous cladded layers during the LMD process cannot lead to the formation of the precipitates in this steel due to slow kinetics of the martensite decomposition. This is different from other maraging steels [15]. However, massive nano precipitates were dispersed in the matrix of the tempered samples (Fig. 3b), which were expected to improve the hardness of the steel by precipitation strengthening. After treating at 550 ℃ for 100 h, the precipitated particles became less but bigger (Fig. 3c). It meant that Ostwald ripening (small particle dissolving, large particle growing) occurred in the alloy during this process. Increasing the softening temperature to 600 ℃, this coarsening phenomenon was more distinct as shown in Fig. 3d.

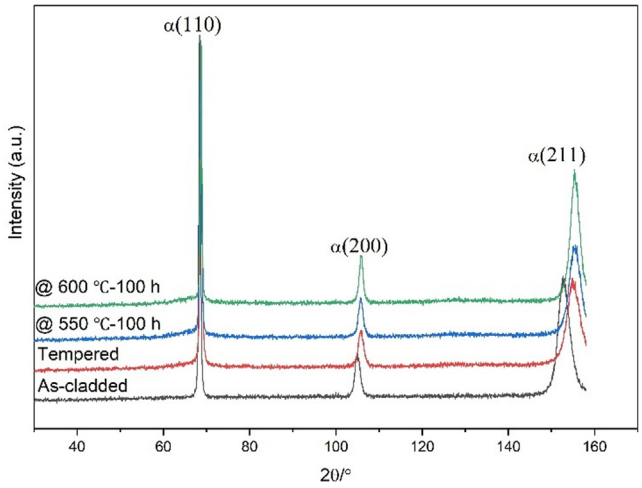

Fig. 2. XRD patterns of NMS at various conditions.

Auger electron spectroscopy (AES) is a useful technique to analyze the chemical composition of small features. Here, it was used to clarify qualitatively the chemical composition of the precipitate particles in the NMS. As shown in Fig. 4, besides Fe, major alloying elements Cr, Mo, Co, Cu and Ni were detected in the AES spectra. Compared to the matrix, significantly higher peak intensity of Mo from the precipitate indicated higher concentration of Mo there. Moreover, absence of carbon peak in the spectra from these precipitate particles implied that they were intermetallic compounds instead of carbides.

In order to quantify the precipitates, TEM with higher resolution was applied. The representative TEM images of the precipitates under different conditions were shown in Fig. 5. ImageJ software was applied to estimate the particle size and fraction from TEM images.

Similar precipitate evolution as observed in the SEM images was found by TEM. Firstly, no precipitate was found in the as-cladded sample (Fig. 5a). However, some black particles, which were suspected to be primary carbide, were distributed on the grain boundary. In addition, some white spots decorated by a small black particle in the center were considered as the nucleation clus-

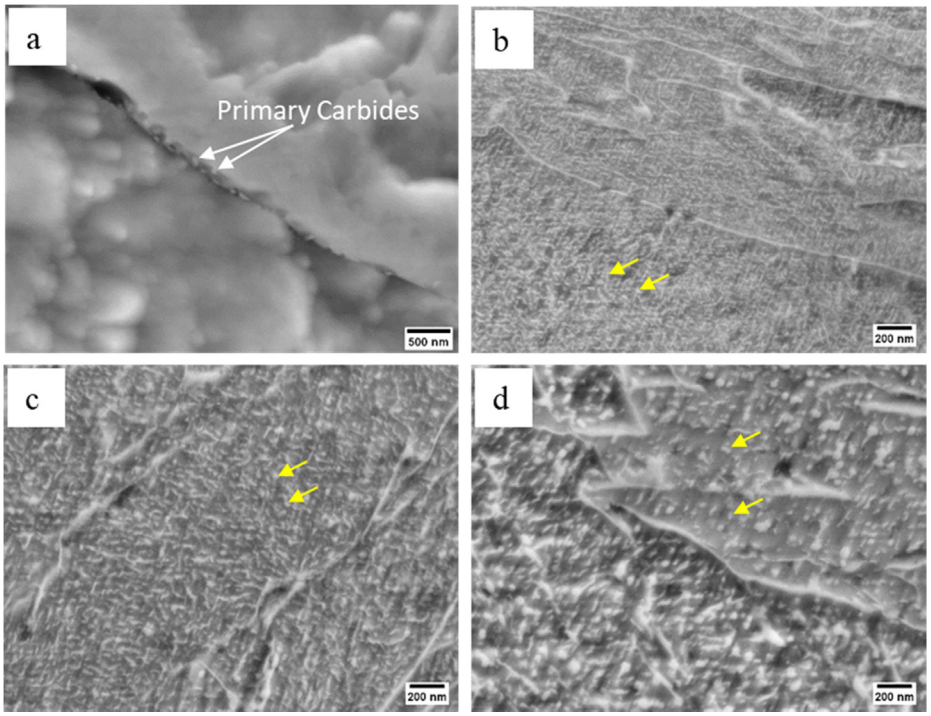

Fig. 3. Secondary electron-SEM images of NMS from the top layer at different conditions: (a) As-cladded; (b) Tempered; (c) Softened at 550 ℃ – 100 h; (d) Softened at 600 ℃ – 100 h.

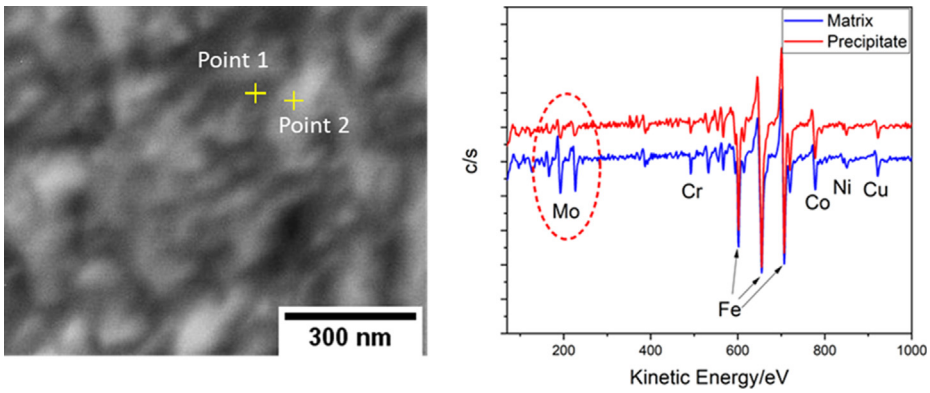

Fig. 4. AES spectra reveals different Mo intensity from the matrix and the precipitates. a) SEM image providing analysis location; b) AES spectra from the matrix (point 1) and precipitate (point 2).

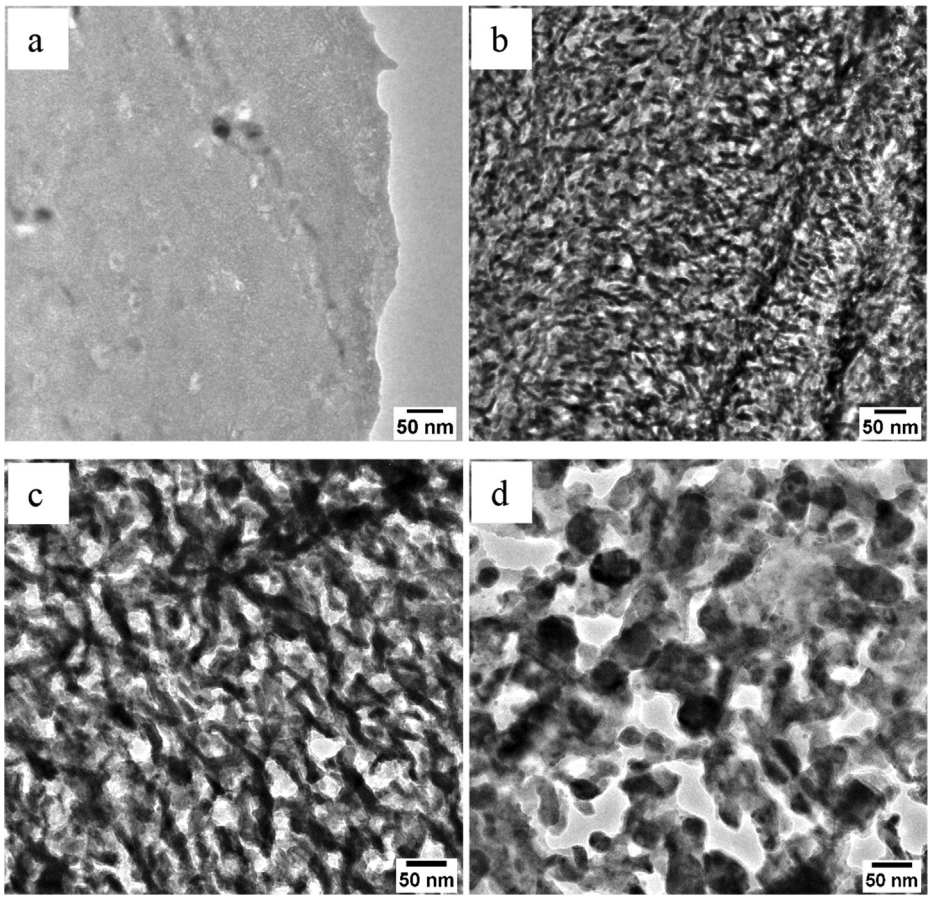

Fig. 5. Representative TEM micrographs of precipitates at different conditions: (a) as-cladded; (b) as-tempered, (c) 550 ℃ – 100 h after tempering, (d) 600 ℃ – 100 h after tempering.

ters of the precipitates. In the tempered sample (Fig. 5b), the particle had a mean diameter of ~ 12 nm. After the softening treatment at 550 ℃ for 100 h, the mean particle diameter increased to ~ 19 nm (Fig. 5c). Increasing the softening temperature to 600 ℃, the corresponding mean diameter was ~ 27 nm averagely. It should be noticed that the amount of the precipitates was relatively constant in the range of ~ 17 vol% during the softening process, which agrees with the Ostwald ripening model [19]. Furthermore, the shape of precipitates changed from needle-like to spherical. This was attributed to the need of lowering the surface energy. At the beginning of precipitation, the precipitates were formed following a certain orientation relationship with the matrix (coherency) in order to reduce the nucleation barrier. However, the precipitates tended to spheroidize at high temperatures in order to lower the overall surface energy.

3.2. Hardness evolution

Generally, coarsening of the precipitates will significantly influence the mechanical properties of alloy. As shown in Fig. 6, the

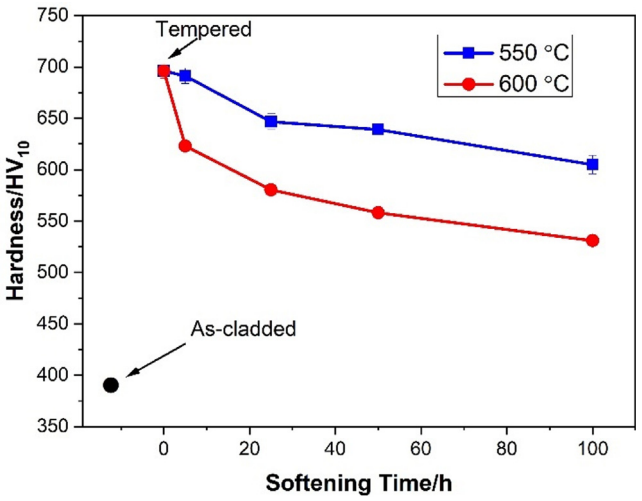

Fig. 6. The hardness evolution of NMS after treated at various conditions.

hardness of NMS was significantly increased from ~ 380 HV to ~ 700 HV after being tempered, attributed to the massive precipitates in the steel and the absence of reverted austenite. In the following softening process, the hardness decreased as expected. The hardness dropped by 12.9 % (to 605 HV) for 550 ℃ and 100 h to 23.7 % (to 531 HV) for 600 ℃ and the same duration. In Ref. [20], the softening resistance of the widely used H13 hot work tool steel produced by laser-beam powder bed fusion (LPBF) was evaluated. For the same duration, the corresponding hardness drop is 12.8 % (to 545 HV) for heating at 550 ℃ and 44.0 % (to 333 HV) at 600 ℃, respectively. Compared to widely used H13 hot tool steel, NMS shows a much higher softening resistance at 600 ℃ and has a higher final hardness after heating at both 550 ℃ and 600 ℃. Softening is mainly attributed to the coarsening of precipitates. From the kinetic perspective, the coarsening rate at higher temperatures should be larger, leading to a faster decrease in the precipitation strengthening effect. Hence, NMS shows a bigger hardness drop at 600 ℃ than that at 550 ℃ (Fig. 6). The influence from other strengthening effects (such as dislocation strengthening, and grain boundary strengthening) is expected to be rather limited.

3.3. Precipitate identification

Identification of precipitate phase in the deposited NMS will help us to understand better the mechanical properties. In the present study, massive precipitates were observed in the heat- treated NMS (Fig. 3). To identify the precipitates, simulation was performed by using Themo Calc software, as illustrated in Fig. 7. As can be seen in Fig. 7a, the matrix phase is supposed to be bcc ferrite at the equilibrium condition of 500–600 ℃. The dominant precipitate is supposed to be C14-Laves phase (Fig. 7b). Compared to C14-Laves phase, other strengthening phases should have a far small mole fraction. Their influence on softening behavior is thus negligible and will not be discussed in this study, although small amount of primary carbide was found in Fig. 5a. Since the peak hardness has been reached after tempering using the optimized heat treatment parameter, it is reasonable to assume that the volume fraction of the Laves phase has reached the maximum value after double tempering at 535 ℃ for 3 h. At 535 ℃, the mole content of the Laves phase was about 14.2 mol % (equivalent to ~ 15.5 vol%) based on the simulation. This agreed roughly with the estimation of precipitate fraction (~17 vol%) from TEM images. In addition, the composition of the C14-Laves phase was also provided by Thermo-Calc (Fig. 7c) simulation. As can be seen, the Mo content in Laves was maintained to be 33.3 mol.%, indicating that the stoichiometry of this C14-Laves phase in NMS is $(Fe, Cr)_2Mo$.

In order to confirm this phase further, a high-resolution TEM (HRTEM) study, as given in Fig. 8, was applied. Fig. 8b is the fast Fourier transform (FFT) image transformed from the rectangle region in Fig. 8a. It indicated that the lattice structure of the precipitates was hexagonal, with lattice parameters of a = 0.468 nm and c = 0.764 nm. This was consistent with the literature [21]. Similarly, the lattice parameter a of the α matrix with bcc structure calculated from the high-resolution image was about 0.2912 nm, which was slightly higher than the standard lattice parameter of ferrite (0.2866 nm) [22]. The orientation relationship between Laves phase and the α matrix was identified to be $[0001]_L//[\bar{1}11]_\alpha$, $(10\bar{1}0)_L//(1\,1\,0)_\alpha$ according to Fig. 8b. The interplanar spacing of $d_{(10\bar{1}0)L}$ and $d_{(1\,1\,0)\alpha}$ is 0.4053 nm and 0.2060 nm, respectively. Hence, the mismatch between $d_{(10\bar{1}0)L}$ and $2d_{(1\,1\,0)\alpha}$ can be calculated and was as small as 1.9 %. The coherent interface with low mismatch will result in low interfacial energy and a consequently low driving force for the growth of the precipitates. This is one of the reasons that the C14-Laves phase is a thermal stable phase and that the steel has an outstanding softening resistance at high temperatures. Furthermore, the coherent interface made the distribution of the precipitate homogeneous in the matrix. This also agreed with the microstructural observation in Fig. 3 and Fig. 5.

4. Discussion

4.1. Precipitate evolution

It is well known that the mechanical properties of an alloy can be significantly influenced by the size and the spacing of precipitates, which can be changed with temperature and time of the heat-treatment [16]. The evolution of the precipitate can be divided into two stages: growth and coarsening [23]. In the first stage, precipitates are nucleated and grow. Large volume fraction of small precipitates contributes to a better strengthening effect. Notice the solutes for precipitating is from the surrounding matrix. The particle size and volume fraction of the precipitates will increase with time until achieving equilibrium. Once peak hardness is reached, the volume fraction of the precipitate will remain constant and then the coarsening starts. According to Ostwald ripening mechanism [19], the large particles with low specific surface area tend to grow at the expense of small particles in this stage. Hence, longer heating (or aging) will lead to an increase of the average particle size, but the volume fraction remains constant.

In the present study, the peak hardness of the tested material has been obtained after being tempered at the optimized conditions. It is reasonable to deduce that the precipitate growth in the tempered material has been finished and the volume fraction of the precipitates is constant after tempering, as confirmed by the observation from TEM. The subsequent evolution of precipitates during the softening treatment is coarsening driven by the interfacial free energy between the particle and matrix. The relationship between particle size and coarsening (softening) time can be described by the widely used Lifshitz-Slyozov-Wagner (LSW) model [910], as given in Eq. (1):

$$r^3 - r_0^3 = \frac{8D\sigma c_\alpha V_m^p}{9RT}t \quad (1)$$

Where r_0: initial radius of the precipitate at time = 0,

r: average radius of the precipitate at time t,
D : diffusion coefficient of the controlling solutes,

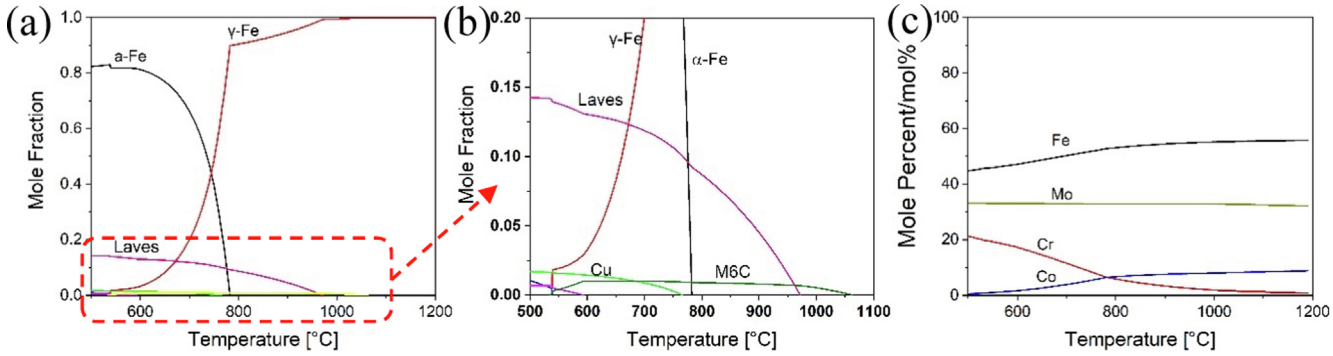

Fig. 7. Prediction of the equilibrium phase in NMS based on simulation using Themo-Calc: (a) the phase evolution as a function of temperature; (b) the zoom-in image; (c) the composition of the C14-Laves phase.

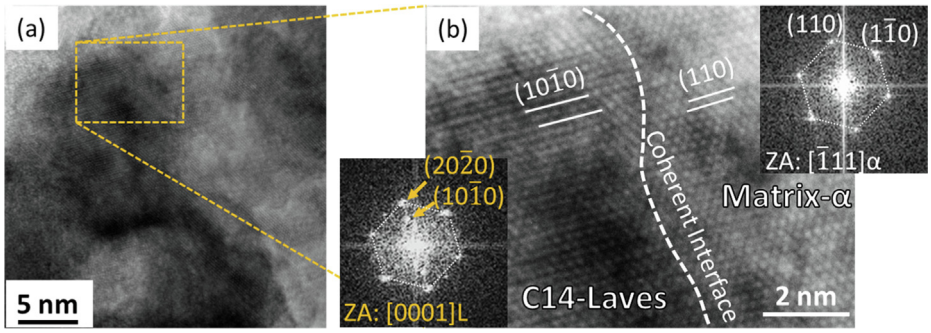

Fig. 8. (a) High-resolution TEM image from the sample treated at 550 ℃ for 100 h; (b) magnified image showing the lattice of the precipitate and the matrix. FFT patterns were obtained from different areas.

σ: interfacial energy per unit area between matrix and precipitate,
c_α solid solubility of the controlling elements in the matrix,
V_m^p: mole volume of the precipitate,
R: gas constant (8.314 J mol^{-1} K^{-1}),
T: temperature in Kelvin.

The values of parameter σ, c_α and V_m^p can be obtained by ThermoCalc software, as given in Table 2. It is clear that the coarsening rate is controlled by the interfacial energy and diffusion coefficient. However, one essential precondition of LSW model is that the fraction of precipitates should be very small (<1 vol%). This is obviously not the case in the present study. Taking the influence of volume fraction into account, a revised LSW relationship has been proposed [24], as shown in Eq. (2):

$$r^3 - r_0^3 = \frac{8D\sigma V_m^p}{9RT} \cdot \frac{c_\alpha(1-c_\alpha)(1+5f)}{(c_p - c_\alpha)^2} t \quad (2)$$

where f is the mole fraction of the precipitates, C_p is the concentration of the controlling element in the precipitates. However, dislocations in the material provide a high-speed path for solute diffusion that might be several orders higher than that in the matrix. The influence of dislocation on diffusion behavior cannot be ignored. In MatCalc software [24], the true diffusion coefficient is described in Eq.(3):

$$D = \pi R_{core}^2 \rho D_{dis} + (1 - \pi R_{core}^2 \rho) D_m \quad (3)$$

Where D_m: diffusivity of the controlling element in matrix,

D_{dis}: diffusivity in the dislocation,
ρ : dislocation density adopted as 10^{14} m^{-2},
R_{core}: radius of dislocation, which is usually considered as the value of Burgers vector of dislocations.

In this study, Mo is the controlling element for precipitate coarsening since there is an abundance of Fe in the matrix. Therefore, C_p = 0.3334, as predicted by Themo-Calc in Fig. 7c. The diffusivity of the controlling element Mo in the bcc-Fe matrix, D_m, is estimated as 4.75 × 10^{-21} and 3.87 × 10^{-20} m^2·s^{-1} at 550 ℃ and 600 ℃, respectively [25]. In the temperature range of 550–600 °C, diffusivity of Mo along the dislocation core can be estimated as $D_{dis} \approx 1 \times 10^5 D_m$ [26]. Then the true diffusion coefficient D of Mo can be calculated by Eq. (3). By using Eq. (2), the radius of the precipitates in NMS is plotted as a function of coarsening time, as shown in Fig. 9. All parameters used in the calculation are summarized in Table 2. As we can see, the calculated particle size agrees well with the experimental observation for 550 ℃. However, it is larger than that of the experimental observation at 600 ℃. This is

Table 2
The adopted parameters in the calculation using revised LSW model.

Diffusion coefficient of Mo in a bcc-Fe matrix at 600 ℃, D_m	3.87 × 10^{-20} m^2/s
Diffusion coefficient of Mo in a bcc-Fe matrix at 550 ℃, D_m	4.75 × 10^{-21} m^2/s
Interfacial energy between matrix and precipitate, σ	0.261512 J/m^2
Mo concentration (atomic fraction) in matrix, c_α	0.0482
Mo concentration (atomic fraction) in the precipitate, c_p	0.3334
Molar volume of precipitate, Vm p	6 × 10^{-6} m^3/mol
Gas constant, R	8.314 J mol^{-1} K^{-1}
Mole fraction, f	0.155
Burgers vector, b	0.248 nm
Shearing modulus, G	76 GPa

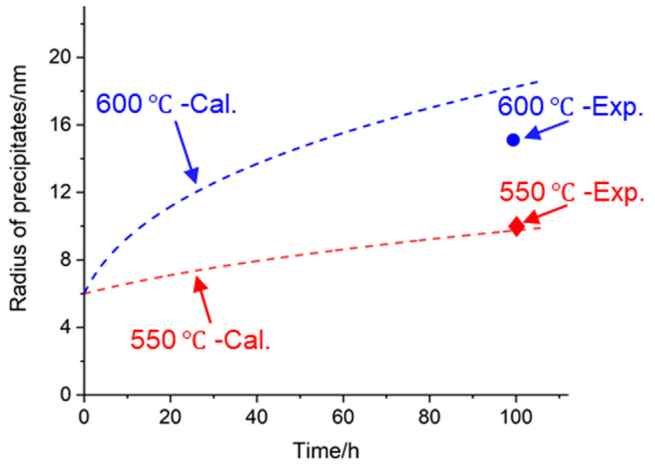

Fig. 9. Coarsening of the precipitates calculated by using Eq. (2) and (3) and comparison with the radius (half of the mean diameter) measured from TEM images at 550 ℃ and 600 ℃.

probably caused by the overestimated dislocation density at the higher temperature. It is worth to mention that the diffusion coefficients D of the controlled elements will largely influence the coarsening rate of precipitates according to the Eq. (2). In the present study, the controlling element Mo has a lower diffusion coefficient compared to other alloying elements, which resulted in the low coarsening rate of the Laves phase and delay the softening of the steel.

4.2. Strengthening mechanism

The factors that determine the strength of alloys include dislocation density, grain boundary strengthening, solution strengthening and precipitation hardening. The alloys fabricated by AM usually have a relatively high dislocation density (in the range of 10^{14} –10^{15} m^{-2} for martensite steels) [2728]. However, in the present study, as-cladded specimens were double-tempered at 535 ℃ for 3 h before the softening treatment. Hence, it is believed that the dislocation density in tempered samples is largely decreased and maintained at an estimated level of $\sim 1 \times 10^{14}$ m^{-2} [29]. Moreover, dislocation lines have not been frequently observed by TEM even in as-cladded samples (Fig. 5a). It is thus expected that the contribution of the dislocations to the strength is similar under different softening conditions in this study. In addition, since the precipitate fraction is maintained at a constant level and the grain size does not grow up significantly, the influence of grain boundary and solid solution on the strength is less important in this case.

It is generally believed that precipitate strengthening due to the interaction between dislocation and precipitate is one of the main strengthening mechanisms in maraging steels [16]. Two well-known models, i.e., shearing and pass-by model (also known as Orowan looping) [30] are often accounted for this behavior, as expressed in Eq. (4) and (5) [3132].

$$\Delta\sigma_{shearing} = \left(\frac{3}{4}\pi\right)^{1/3} \cdot \frac{\pi\sigma}{2b} \cdot f_v^{1/3} \tag{4}$$

$$\Delta\sigma_{bypassing} = \frac{Gb}{\sqrt{\frac{2\pi}{3f_v}} \cdot \frac{\bar{d}_p}{2}} \tag{5}$$

Where f_v: volume fraction of the precipitate,

$\bar{d}_p$: average diameter of precipitate,
b : Burgers vector of Fe (=0.248 nm),
G: shear modulus.

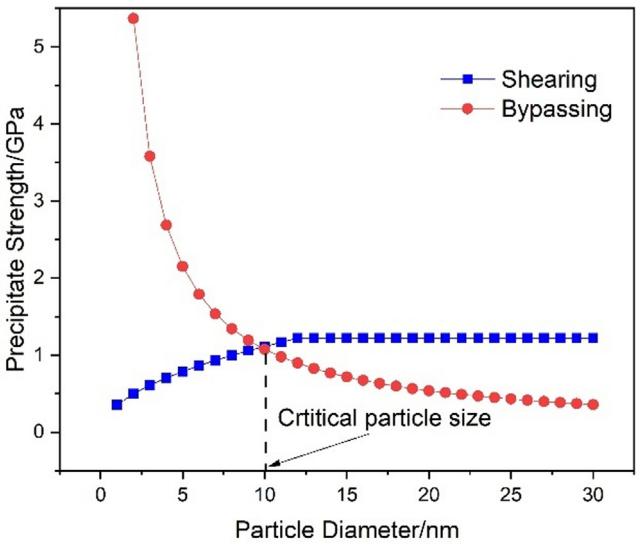

Fig. 10. Precipitate strengthening effect as a function of particle diameter using shearing and bypassing model.

Equation (4) applies when the volume fraction of precipitates f_v is constant. In the initial stages, the strengthening effect is proportional to size and volume of the particle and can be expressed as Eq. (6) [33].

$$\Delta\sigma_{shearing} = A\sqrt{\bar{d}_p f_v} \tag{6}$$

where A is a constant, which can be calculated at the start condition of Equation (4). Combining Equation (4), (5) and (6), the competition between shearing and bypassing is revealed in Fig. 10. Some parameters adopted in this calculation are also presented in Table 2. How dislocations interact with the precipitate is dependent on the size of precipitates [31]. When the particle is smaller than the critical size, $\Delta\sigma_{shearing}$ is smaller than $\Delta\sigma_{bypassing}$, which means dislocations move easier by shearing than by bypassing. Once the particle size reaches the critical value, bypassing will be governing. In our case, the critical size of the precipitates in NMS is about ~ 10 nm (Fig. 10) which is smaller than the average particle size in tempered NMS (~12 nm), meaning that bypassing mechanism is dominant and the strengthening effect of precipitates in the softened sample should be calculated by Eq. (5).

After softening at 550 ℃ for 100 h, the particle diameter in NMS increases from ~ 12 nm to ~ 19 nm. Based on Eq. (5) and Fig. 10, precipitate strengthening is decreased from 847 MPa to 537 MPa. The estimated decrease of the yield strength is ~ 310 MPa. For non-work hardening materials [34], there is a proportional relationship between yield strength and Vickers hardness, $\Delta H(Hv) \approx 0.3\Delta\sigma_y$. Hence, at 550 °C, the estimated decrease of hardness is $\Delta H_{550} \approx 93$, which agrees with the experimental hardness decrease ($\Delta H_{550} = 95$ HV). Similarly, after treating at 600 ℃ for 100 h, the calculated decrease of the hardness is $\Delta H_{600} = 151$ HV, which roughly agrees well with the experimental one ($\Delta H_{600} =$ 169 HV).

5. Conclusions

A newly developed maraging steel (NMS) was cladded on a tool steel substrate by directed energy deposition technique. The softening resistance of the cladded NMS with optimized tempering was evaluated at high temperatures. Based on the experimental results and numerical simulations, the main conclusions are presented as followed:

(1) Defect-free NMS samples were successfully fabricated by LMD technique. No retained or reverted austenite phase was found in the cladded sample by the XRD technique before and after tempering. C-14 Laves nanoparticles formed during tempering provide strong precipitate strengthening effect.
(2) A good softening resistance of the material was revealed at 550 ℃ and 600 ℃ for 100 h. This is attributed to the low coarsening rate of the precipitates, i.e., C-14 Laves phase particles. Two factors were responsible for this: the coherent interface with small mismatch between Laves phase and the matrix, and the low diffusion coefficient of the controlled element (Mo).
(3) The coarsening behavior of the precipitates as a function of temperature is simulated by the revised LSW model, which is successful in general. The simulated particle size agrees well with the experimental observation at 550 ℃, while it is slightly larger than the experimental one at 600 ℃.
(4) The hardness drop due to precipitate coarsening during softening was also estimated by the precipitate strengthening models. The estimated hardness drop is consistent with the experimental observation at both 550 ℃ and 600 ℃.

Data availability

The authors do not have permission to share data.

Declaration of Competing Interest

The authors declare that they have no known competing financial interests or personal relationships that could have appeared to influence the work reported in this paper.

Acknowledgements

This study is supported by Production Area of Advance, Chalmers University of Technology, China Scholarship Council, Uddeholms AB, Sweden and ASSAB Tooling Technology, China.

References

[1] M. Naderi, Hot Stamping of Ultra High Strength Steels (Doctoral Thesis), Rwth Aachen University, 2007.
[2] G. Roberts, G. Krauss, R. Kennedy, Tool Steels, 5th ed., ASM International, Materials Park, 1998.
[3] D. Mellouli, N. Haddar, A. Köster, H.F. Ayedi, Hardness effect on thermal fatigue damage of hot-working tool steel, Eng. Fail. Anal. 45 (2014) 85–95.
[4] J. Sjöström, J. Bergström, Thermal fatigue testing of chromium martensitic hot-work tool steel after different austenitizing treatments, J. Mater. Process. Technol. 153 (2004) 1089–1096.
[5] M. Muro, G. Artola, A. Gorriño, C. Angulo, Wear and Friction Evaluation of Different Tool Steels for Hot Stamping, Adv. Mater. Sci. Eng. 2018 (2018) 1–11.
[6] A. Vikhareva, G. Macêdo, L. Pelcastre, et al., High temperature tribological behaviour of additively manufactured tool material for applications in press hardening", Wear 477 (2021) 203859.
[7] E.V. Pereloma, A. Shekhter, M.K. Miller, S.P. Ringer, Ageing behaviour of an Fe–20Ni–1.8 Mn–1.6 Ti–0.59 Al (wt%) maraging alloy: clustering, precipitation and hardening, Acta Mater. 52 (19) (2004) 5589–5602.
[8] J.M. Pardal, S.S.M. Tavares, V.F. Terra, M.R. Da Silva, D.R. Dos Santos, Modeling of precipitation hardening during the aging and overaging of 18Ni–Co–Mo–Ti maraging 300 steel, J. Alloy. Compd. 393 (1–2) (2005) 109–113.
[9] I.M. Lifshitz, V.V. Slyozov, The kinetics of precipitation from supersaturated solid solutions, J. Phy. Chem. Solids 19 (1-2) (1961) 35–50.
[10] C. Wagner, Theory of precipitate change by redissolution, Z. Elektrochem 65 (1961) 581–591.
[11] T. Allam, K.G. Pradeep, P. Köhnen, et al., Tailoring the nanostructure of laser powder bed fusion additively manufactured maraging steel, Addit. Manuf. 36 (2020) 101561.
[12] F.F. Conde, J.A. Avila, J.P. Oliveira, et al., Effect of the as-built microstructure on the martensite to austenite transformation in a 18Ni maraging steel after laser-based powder bed fusion, Addit. Manuf. 46 (2021) 102122.
[13] S. Dehgahi, M. Sanjari, M.H. Ghoncheh, et al., Concurrent improvement of strength and ductility in heat-treated C300 maraging steels produced by laser powder bed fusion technique, Addit. Manuf. 39 (2021) 101847.
[14] P. Kürnsteiner, M.B. Wilms, A. Weisheit, P. Barriobero-Vila, E.A. Jägle, D. Raabe, Massive nanoprecipitation in an Fe-19Ni-xAl maraging steel triggered by the intrinsic heat treatment during laser metal deposition, Acta Mater. 129 (2017) 52–60.
[15] E. Jägle, Z. Sheng, P. Kürnsteiner, S. Ocylok, A. Weisheit, D. Raabe, Comparison of maraging steel micro- and nanostructure produced conventionally and by laser additive manufacturing, Materials 10 (1) (2017) 8.
[16] K. Li, L. Wei, B. An, B. Yu, R.D.K. Misra, Aging phenomenon in low lattice-misfit cobalt-free maraging steel: Microstructural evolution and strengthening behavior, Mater. Sci. Eng. A 739 (2019) 445–454.
[17] P.P. Sinha, D. Sivakumar, N.S. Babu, K.T. Tharian, A. Natarajan, Austenite reversion in 18 Ni Co- free maraging steel, Steel Res. 66 (11) (1995) 490–494.
[18] U.K. Viswanathan, G.K. Dey, V. Sethumadhavan, Effects of austenite reversion during overageing on the mechanical properties of 18 Ni (350) maraging steel, Mater. Sci. Eng. A 398 (1-2) (2005) 367–372.
[19] H. Gleiter, Chapter 9: Microstructure, in: Physical Metallurgy, 4th ed., North-Holland, 1996, pp. 843-942.
[20] M. Wang, W. Li, Y. Wu, S. Li, C. Cai, S. Wen, Q. Wei, Y. Shi, F. Ye, Z. Chen, High-Temperature Properties and Microstructural Stability of the AISI H13 Hot-Work Tool Steel Processed by Selective Laser Melting, Metall. Mater. Trans. B 50 (1) (2019) 531–542.
[21] S. Zhang, H. Fang, M.E. Gramsma, et al., Autonomous Filling of Grain-Boundary Cavities during Creep Loading in Fe-Mo Alloys, Metall. Mater. Trans. A Phys. Metall. Mater. Sci. 47 (10) (2016) 4831–4844.
[22] S.J. Lee, Y.K. Lee, Quantitative analyses of ferrite lattice parameter and solute Nb content in low carbon microalloyed steels, Scr. Mater. 52 (10) (2005) 973–976.
[23] Z. Guo, W. Sha, Quantification of precipitation hardening and evolution of precipitates, Mater. Trans. 43 (6) (2022) 1273–1282.
[24] Z. Guo, W. Sha, Quantication of precipitation kinetics and age hardening of Fe–12Ni–6Mn alloy during overaging, Mater. Sci. Technol. 18 (5) (2002) 529–533. https://www.matcalc.at/wiki/doku.php?id=techpapers:precipitation:diffusion.
[25] H. Nitta, T. Yamamoto, R. Kanno, et al., Diffusion of molybdenum in α-iron, Acta Mater. 50 (16) (2002) 4117–4125.
[26] https://www.matcalc.at/wiki/doku.php?id=techpapers:precipitation:diffusion.
[27] M. Alnajjar, F. Christien, C. Bosch, et al., In-situ neutron diffraction study of wrought and selective laser melted maraging stainless steels, Mater. Charact. 172 (2021) 110840.
[28] W. Zhong, N. Sridharan, D. Isheim, et al., Microstructures and mechanical properties of a modified 9Cr ferritic-martensitic steel in the as-built condition after additive manufacturing, J. Nucl. Mater. 545 (2021) 152742.
[29] J. Pešička, R. Kužel, A. Dronhofer, et al., The evolution of dislocation density during heat treatment and creep of tempered martensite ferritic steels, Acta Mater. 51 (16) (2003) 4847–4862.
[30] E. Orowan, Discussion on Internal Stresses, in: Symp. Internal Stresses in Metals and Alloys (The Institute of Metals, London, 1948), pp. 451–453.
[31] M.A. Meyers, K.K. Chawla, Mechanical behavior of materials, Cambridge University Press, 2008.
[32] M.F. Ashby, Results and consequences of a recalculation of the frank-read and the orowan stress, Acta Metall. 14 (1966) 679–683.
[33] V. Gerold, H. Haberkorn, On the critical resolved shear stress of solid solutions containing coherent precipitates, Phys. Status Solidi 16 (1966) 675–684.
[34] P. Zhang, S.X. Li, Z.F. Zhang, General relationship between strength and hardness, Mater. Sci. Eng. A 529 (2011) 62–73.